Distributed Multi-GNSS Timing and Localization for Nanosatellites

Vincent Giralo, *Space Rendezvous Lab, Stanford University, Stanford, CA, United States*
Simone D'Amico, *Space Rendezvous Lab, Stanford University, Stanford, CA, United States*

BIOGRAPHIES

Vincent Giralo is a Ph.D. student in Stanford University's Space Rendezvous Laboratory. He graduated from Bucknell University with a Bachelor of Science degree in mechanical engineering, as well as Stanford University with a Master of Science degree in Aeronautics and Astronautics. His current research focuses on using GNSS technology for precise relative navigation of multiple small satellites. This includes development of algorithms for integer ambiguity resolution to accomplish this task in real-time, given the onboard constraints. His main research project is the Distributed multi-GNSS Timing and Localization system (DiGiTaL) under development for the NASA Small Satellite Technology Development Program in cooperation with NASA Goddard Space Flight Center and Tyvak Nanosatellite Systems.

Simone D'Amico is an Assistant Professor of Aeronautics and Astronautics at Stanford University, a Terman Faculty Fellow of the School of Engineering, Founder and Director of the Space Rendezvous Laboratory, and Satellite Advisor of the Student Space Initiative, Stanford's largest undergraduate organization. He received his B.S. and M.S. from Politecnico di Milano and his Ph.D. from Delft University of Technology. Before Stanford, Dr. D'Amico was at DLR, German Aerospace Center, where he gave key contributions to the design, development, and operations of spacecraft formation-flying and rendezvous missions such as GRACE (United States/Germany), TanDEM-X (Germany), and PRISMA (Sweden/Germany/France), for which he received several awards. Dr. D'Amico's research lies at the intersection of advanced astrodynamics, GN&C, and space system engineering to enable future distributed space systems. He has over 140 scientific publications including conference proceedings, peer-reviewed journal articles, and book chapters. He has been Programme Committee Member (2008), Co-Chair (2011), and Chair (2013) of the International Symposium on Spacecraft Formation Flying Missions and Technologies. He is Programme Committee Member of the International Workshop on Satellite Constellations and Formation Flying since 2013. He is a member of the Space-Flight Mechanics Technical Committee of the American Astronautical Society and Associate Editor of the Journal of Guidance, Control, and Dynamics.

ABSTRACT

The way humans conduct spaceflight is being revolutionized by two key trends. The first trend is the distribution of payload tasks among multiple coordinated units, referred to as Distributed Space Systems (DSS), which allow for advances in Earth and planetary science, on-orbit servicing, and space situational awareness. To mimic a gigantic spacecraft with adjustable baselines, DSS require precise knowledge of the relative states of each orbiting satellite. Centimeter-level relative positioning precision can be obtained from Global Navigation Satellite Systems (GNSS) using differential carrier-phase techniques, where synchronous measurements are shared between spacecraft and error-cancelling combinations of various data types are formed to create precise baseline knowledge. The second trend is spacecraft miniaturization, whereby micro- and nanosatellites are transitioning from being merely educational tools to a viable scientific platform. The recent advances in distribution and miniaturization motivate the Distributed Multi-GNSS Timing and Localization (DiGiTaL) system described in this paper. DiGiTaL is intended to provide nanosatellite swarms with unprecedented centimeter-level navigation accuracy in real-time and nanosecond-level time synchronization through the integration of a multi-constellation GNSS antenna and receiver, a Chip-Scale Atomic Clock (CSAC), and an Inter-Satellite Link (ISL). This paper describes DiGiTaL's hardware and software design, architecture, and algorithms in detail. Specifically, the design is documented through the major trades conducted on the potential hardware, considering its compatibility with the CubeSat size and power resources, modern GNSS signal support, and flight heritage. Next, the performance of the candidate receivers is characterized in terms of measurement noise to verify their capability to perform precise relative navigation through carrier-phase differential GNSS at the centimeter level. The navigation software and core algorithms are described with their rationale. In order to render the distributed navigation system computationally tractable, the states of all swarming spacecraft are grouped into subsets through a connected graph. Differential

GNSS is only performed between spacecraft within each subset by a precise orbit determination module with integer ambiguity resolution in real-time. The resulting precise orbits are then exchanged and fused by the swarm orbit determination module removing the necessity to form single- and double-differenced carrier-phase measurements between all spacecraft of the swarm. Finally, the DiGiTaL architecture is integrated into CubeSat avionics and tested with all key hardware in the loop using the Stanford's GNSS and Radiofrequency Autonomous Navigation Testbed for DSS (GRAND). For the first time, this paper shows the capability to perform centimeter-level precise relative navigation using commercial-off-the-shelf CubeSat hardware for a swarm of multiple spacecraft.

INTRODUCTION

Distributed Space Systems (DSS) use multiple spacecraft to achieve goals that would be difficult or impossible to achieve with a monolithic spacecraft. The resulting breakthrough applications can be categorized in areas such as space infrastructure and development (e.g., on-orbit servicing and assembly [1]), astronomy and astrophysics (e.g., exoplanet imaging [2]), and planetary and earth science (e.g., synthetic aperture radar interferometry [3]) to name a few. To accomplish these objectives, DSS require precise knowledge of both the absolute and relative orbits of each spacecraft in the system. Global Navigation Satellite Systems (GNSS), such as the Global Positioning System (GPS), Galileo, and BeiDou, are the most widely used method for providing this type of precision navigation. For a single spacecraft, absolute positioning accuracies of 50 cm have been demonstrated onboard spacecraft in real-time [4]. For relative navigation between multiple spacecraft, differential GNSS (dGNSS) techniques can be exploited to cancel out common errors and create highly precise relative state estimates [5,6].

GPS relative navigation has been successfully demonstrated numerous times in spacecraft formation-flying on science missions such as NASA/DLR's Gravity Recovery and Climate Experiment (GRACE) [7,8], DLR's TerraSAR-X Add-on for Digital Elevation Measurement (TanDEM-X) [9,10], and NASA's Magnetospheric Multi-Scale (MSS) mission [11,12]. In contrast to the ground-based approach of these missions, GPS relative navigation has also been pushed to high levels of autonomy on technology demonstration missions like the Swedish Space Corporation's Prototype Research Instruments and Space Mission technology Advancement (PRISMA) mission [13,6,14] and Canada's CanX-4/5 [15,16]. By exchanging GPS measurements between cooperatively orbiting spacecraft, these missions have been able to achieve relative navigation solutions with unprecedented precision onboard. PRISMA, launched in 2010, used an onboard Extended Kalman Filter (EKF) with dGNSS to demonstrate precise navigation capabilities between two small satellites, one active and the other passive, allowing for less than 10 cm of relative positioning error (3D, root mean square) in real-time for most mission scenarios [17].

While these missions demonstrated high navigation performance, several shortcomings of this technology need to be overcome to meet the challenging requirements of future miniature DSS. First, each of these missions was restricted to a binary formation employing a fully centralized master-slave architecture. A direct extension of the algorithms from missions like PRISMA is computationally inefficient for large swarms due to the number of differential carrier-phase measurements that need to be processed between each pair of satellites. Second, the carrier-phase biases are typically estimated as float numbers onboard due to computational complexity and lack of robustness in accurately fixing these values. However, being able to correctly solve for the integer-valued ambiguities can improve the achievable accuracy to the sub-centimeter level [5]. Traditional methods of Integer Ambiguity Resolution (IAR), such as the Least-Squares Ambiguity Decorrelation Adjustment (LAMBDA) method, require an intensive search algorithm due to the integer constraint of the ambiguities. This process is computationally expensive without a guarantee of correctly fixing the values, which could lead to severe degradation of the navigation solution [18]. One method to aid in fixing these values is to extend the range of GNSS signals being processed by the navigation system. In fact, previous missions have only used GPS, and its usage was limited to L1 and rarely L2. Extending beyond single-constellation, single-frequency measurements to include signals from multiple constellations such as GPS, Galileo, and BeiDou, as well as the multiple frequencies available from each, allows for a variety of wide-lane combinations to be made that aids in ambiguity fixing. The use of multiple constellations also increases signal availability, allowing for more accurate navigation solutions due to the increased number of measurements being processed.

As micro- and nanosatellites transition from being merely an educational tool to a viable scientific platform, many small satellite-based distributed mission concepts have been proposed [19]. For example, the CubeSat Proximity Operations Demonstration (CPOD) will demonstrate rendezvous, proximity operations and docking (RPOD) using two 3-unit (3U) CubeSats weighing approximately 5 kg [20]. Due to the power, volume, mass, and cost constraints of small satellite systems such as CPOD, space-hardened receivers like the BlackJack [21] and the Integrated GPS Occultation Receiver (IGOR) [22] are not feasible options for onboard navigation. Therefore, Commercial-Off-The-Shelf (COTS) receivers are used as a viable alternative. CanX-4 and CanX-5, both 8U CubeSats, demonstrated precision relative navigation using GPS measurements on nanosatellites, showing formal covariance bounds and measurement residuals consistent with positioning accuracies of 10 cm [23].

To address the limitations described above while meeting nanosatellite constraints, this work presents the Distributed Multi-GNSS Timing and Localization (DiGiTaL) system. DiGiTaL provides nanosatellite formations with unprecedented centimeter-level navigation accuracy in real-time and nanosecond-level time synchronization through the integration of a multi-constellation GNSS receiver, a Chip-Scale Atomic Clock (CSAC), and an Inter-Satellite Link (ISL). These COTS hardware units were selected due to their small footprints and low power consumption. The DiGiTaL payload has a 0.5U CubeSat form factor, with a maximum power requirement of 3W and a mass of 225g. To help meet the strict navigation requirements of future miniaturized distributed space systems, DiGiTaL exploits powerful error-cancelling combinations of synchronous GNSS carrier-phase measurements which are exchanged between the swarming nanosatellites through a peer-to-peer decentralized network which exploits the connectivity of the graph. A reduced-dynamics estimation architecture onboard each individual nanosatellite processes the resulting millimeter-level noise measurements to reconstruct the full formation state with high accuracy. This system is under development at Stanford University in partnership with Goddard Space Flight Center (GSFC) and Tyvak Nanosatellite Systems as part of the NASA Small Spacecraft Technology Program [24].

Following this introduction, an overview of the system architecture is presented. This section describes each hardware component of the DiGiTaL payload, as well as the selected models of the payload prototype. The software architecture is then presented, where the navigation algorithms are detailed. The final section shows a hardware-in-the-loop (HIL) testcase in Stanford's GRAND testbed [25], where the DiGiTaL prototype is evaluated, demonstrating the ability to achieve centimeter-level relative positioning solutions in a swarm of four nanosatellites.

PROJECT OVERVIEW

DiGiTaL is designed to provide nanosatellite formations with unprecedented centimeter-level navigation accuracy in real-time and nanosecond-level time synchronization to enable advanced swarm missions that have strict navigational requirements. This is accomplished by expanding the state of the art from GPS-only to multiple constellations for onboard dGNSS, adding the benefit of signals at multiple frequencies to increase the robustness of IAR. Also, with the push from binary formations to arbitrarily sized swarms, new algorithms were developed for precise orbit determination to retain the achievable precision from dGNSS throughout the swarm without the associated computational overhead.

To allow for compatibility with most micro- and nanosatellites, the DiGiTaL payload has a 0.5U CubeSat volume footprint which includes multi-GNSS receiver and antenna, CSAC, ISL, and a dedicated flight computer. Excluding the ISL radio, DiGiTaL's integrated hardware produces a maximum power requirement of 3W, with a mass of 225g. Figure 1 depicts a block diagram of the DiGiTaL hardware architecture, which is identical on each spacecraft of the swarm.
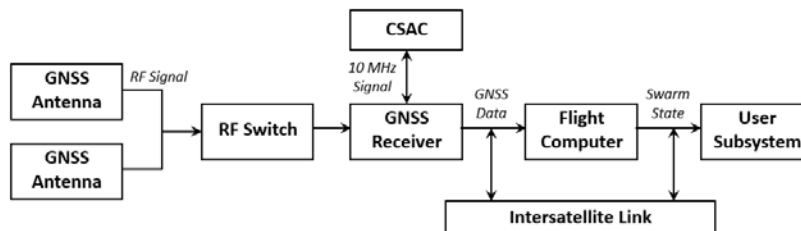

Figure 1: High-level schematic of the DiGiTaL navigation payload.

Two GNSS antennas acquire radiofrequency (RF) signals and point in anti-parallel directions to create near-omnidirectional coverage. The signals then pass through an RF switch, which selects the most favorable antenna (zenith-pointing in LEO) based on available attitude information. The GNSS receiver is conditioned by a CSAC to improve time-to-first-fix and synchronization capabilities throughout the swarm during GNSS outages or contingencies. The raw measurements generated by the GNSS receiver are passed to the local flight computer and to the remote DiGiTaL units through the ISL. The output of differential GNSS processing and swarm orbit determination are delivered to the onboard users.

GNSS Antenna System

The GNSS antenna for DiGiTaL was selected through a survey of COTS models prioritizing small form factor, partial flight heritage, and compatibility with available GNSS signals. A detailed list of the requirements and an extract of the surveyed antennas is given in Table 1.

Table 1: Survey of COTS antenna models. Requirements for specifications are listed in the first row, with individual antenna specs listed below.

Model	Manufacturer	Dimensions [mm]	Mass [g]	Signal Support	Noise [dB]	Gain at Receiver [dB]
Requirement	-	*Max dim. <100*	*200*	*L1, L2, E1, B1*	*<3*	*+15 to +35*
G3Ant-2XXX	Antcom	68.81 x 17.3	184	L1, E1, B1	3	+33
G3Ant-3XXX	Antcom	88.9 x 21.89	256	L1, E1, B1	3	+33
G5Ant-42XXX	Antcom	119.38 x 22.8	227	L1, L2, E1, B1	3	+33 to +35
TW3870E	Tallysman	60 x 15.17	75	L1, L2, E1, B1	2	+35
TW3972E	Tallysman	60 x 14.9	75	All but E6, B3	2.5	+35
GNSS-303L	NovAtel	89.6 x 17.53	340	All	3	+26 to + 30
GNSS-303L-A	NovAtel	119.38 x 76.2	272	All	3	+26 to + 30

*All signals refer to L1, L2, L5, E1, E5a, E5b, AltBOC, E6, B1, B2, B3

Based on the survey, the Tallysman TW3972E Embedded Triple Band GNSS Antenna [26] was selected. This antenna meets the functional requirements (see Table 1, first row), while minimizing mass (see Table 1, fourth column). Previous models of this antenna have been qualified for spaceflight, giving confidence in this antenna's ability to be used on nanosatellites. Two of these antennas are connected to the receiver through an RF switch. Using input from the spacecraft's Attitude Determination and Control System (ADCS), the antenna with the maximum scalar product between zenith and antenna boresight is chosen, and the signals acquired from that antenna are sent to the receiver.

GNSS Receiver

The GNSS receiver for DiGiTaL was selected through a survey of COTS models prioritizing GPS, Galileo and BeiDou compatibility, low mass and form-factor, and the ability to be conditioned by an external reference clock. An extract of the survey results is shown in Table 2.

Table 2: COTS GNSS receiver survey. Design requirements are listed in the first row, with specifications on each receiver listed in subsequent rows.

Model	Manufacturer	Dimensions [mm]	Mass [g]	Signal Support	External Frequency	Power Consumption [W]
Requirement	-	*Max dim. < 100*	*100*	*L1, L2, E1, B1*	*Yes*	*3W*
AsteRx4	Septentrio	82 x 61	55	All*	Yes	3
OEM615	NovAtel	71 x 46	24	L1, L2, L5, E1, B1	No	1
OEM628	NovAtel	100 x 60	37	All but E6, B3	Yes	1.3
TR-G2T	Javad	66 x 57	34	L1, L2, L5, E1, E5a	No	1.6
TRE-G3T	Javad	100 x 80	77	All but B3	Yes	3.6

*All signals refer to L1, L2, L5, E1, E5a, E5b, AltBOC, E6, B1, B2, B3

Based on the survey, the NovAtel OEM628 High Performance GNSS Receiver [27] was chosen. The NovAtel receiver has a small form-factor and power consumption, which are ideal characteristics for a nanosatellite platform. This receiver is also compatible with all current GNSS constellations and frequencies and can be conditioned via an external reference frequency. Also, predecessor NovAtel OEM models have regularly flown on CubeSats before.

A key metric that is used to analyze the performance of the GNSS receiver is the noise of its raw measurements. This is quantified through a zero-baseline test, which was performed on the NovAtel in the GRAND testbed at Stanford [25]. The zero-baseline test uses a GNSS signal simulator to run two identical tests with the same receiver. By double-differencing the measurements from each test, the noise of the receiver can be isolated. Figure 2 shows the resulting noise of both the pseudorange and carrier-phase measurements, as well as an analytical model presented by Ward [28]. This receiver has pseudorange noise at the decimeter level, which is much lower than predicted by the model. More importantly, the carrier-phase noise is at the millimeter level. These low noise figures represent the lower bound on achievable navigation performance when using dGNSS. As a consequence, the selected receiver was deemed capable of meeting the accuracy requirements of DiGiTaL. It is interesting to note that BeiDou residuals are separated into two distinct groups in a bimodal distribution. In fact, the plotted range of C/N_0 between 37.5 dB-Hz and 40 dB-Hz represents the geostationary satellites (PRNs 1-5) and the inclined geosynchronous satellites (PRNs 6-10), while the range between 42 dB-Hz and 44 dB-Hz is associated with the Medium Earth Orbit (MEO) satellites.
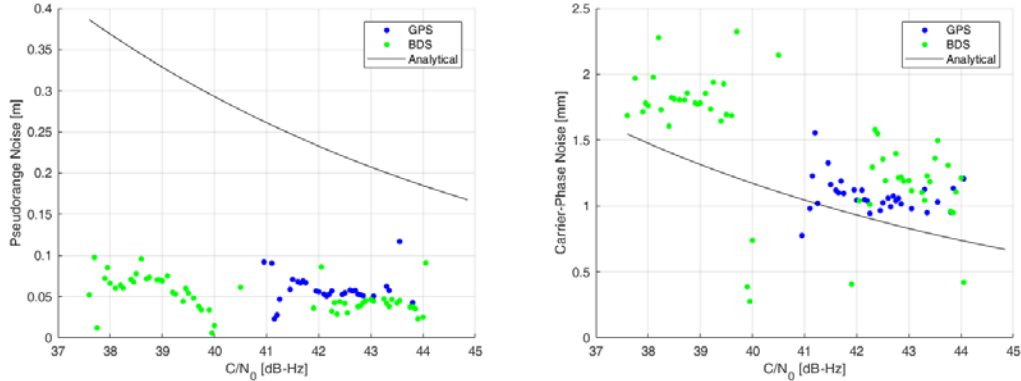
Figure 2: Pseudorange (left) and carrier-phase (right) measurement noise on NovAtel OEM628.

Chip-Scale Atomic Clock

Synchronous measurements must be taken across multiple GNSS receivers to perform dGNSS. This requirement is even stricter in orbit due to the high speeds (~km/s) and resulting Doppler shift with peaks of 45kHz (10min time-to-first-fix). In DiGiTaL, time-synchronization is aided through the use of a CSAC, which also helps to reduce the impact of clock drift in GNSS-impaired scenarios. A survey conducted for COTS CSACs is presented in Table 3 prioritizing size and power constraints. The selected clock is a Low Power Miniature RSR CSAC manufactured by Jackson Labs [29], which provides a 10 MHz reference frequency.

Table 3: Survey of COTS CSACs, including dimensions and power consumption

Model	Manufacturer	Dimensions [mm]	Power Consumption [W]
Requirement	-	Max dim. < 100	1
CSAC GPSDO	Jackson Labs	63 x 76 x 17	1-1.4
HD CSAC GPSDO	Jackson Labs	50 x 63 x 17	<1.25
HC CSAC LP	Jackson Labs	50 x 63 x 17	<0.55
LN CSAC GPSDO	Jackson Labs	98 x 76 x 22	5
RSR CSAC	Jackson Labs	40 x 58 x 17	0.41
CSAC GPSDO	Aventas	50 x 63 x 17	1-1.4
Dev Kit	Microsemi	Not available	0.12

Flight Computer

The DiGiTaL payload processing capabilities are inherited from the CPOD mission [20], including two flatsat development boards from Tyvak Nanosatellite Systems. These platforms integrate the DiGiTaL components during testing, including the NovAtel OEM628 receiver, the 800 MHz Endeavor flight microprocessor, and a UHF radio for communication between the two units. Figure 3 shows a photo of the two boards at Stanford, highlighting the key elements, as well as a schematic of the flatsat architecture. The components which have not been highlighted aid in the interfacing between the flight computer and the hardware through a secondary computer for command and data handling (C&DH).
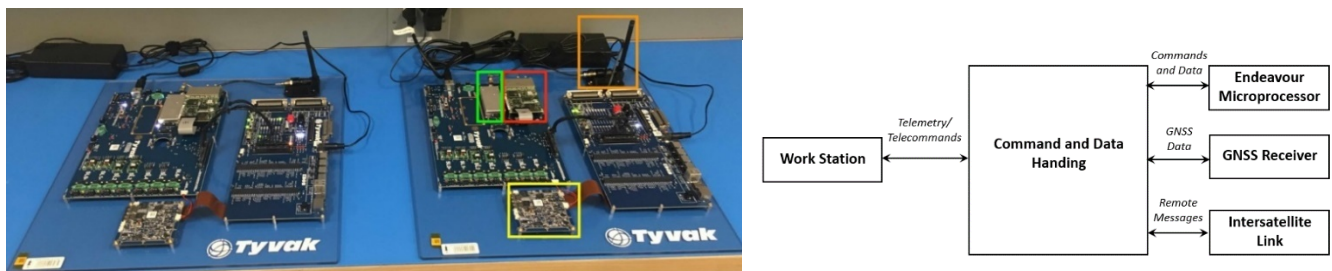

Figure 3: Two prototype DiGiTaL units (left), including the Endeavour flight processor (yellow), the UHF radio (green), the NovAtel receiver (red), and the ISL antenna (orange). A schematic of the flatsat (right) shows interactions between hardware units.

The microprocessor houses the navigation algorithms for DiGiTaL which are written in C/C++. The use of the flight computer allows for demonstration and profiling of the software in real-time. Specifications for the flatsat processors and UHF radio are given in Table 4.

Table 4: Specifications of the Tyvak flatsats used in the DiGiTaL prototype.

Onboard Processors		UHF Radio	
Command & Data Handling Processor		Frequencies	400-470 MHz
Architecture	ARM9		800-930 MHz
Clock speed	400 MHz	Data Rates	1.2-250 kbps
Power Consumption	< 0.2 W	*Power Consumption*	
Endeavour Processor		RF TX	Up to 2 W
Architecture	ARM Cortex A8+	DC TX	7 W
Clock Speed	800 MHz	DC RX	0.130 W
Mass	610 g	Mass	20 g
Volume	83 x 83 x 53 mm	Volume	32 x 87 x 8 mm
Power Consumption	< 1 W	Power Consumption	< 1.3 W

SOFTWARE ARCHITECTURE AND ALGORITHMS

The DiGiTaL system is designed to provide a swarm of small satellites with cm-level relative positioning accuracy between each spacecraft. This is accomplished by utilizing dGNSS in an Extended Kalman Filter (EKF), where datatypes from multiple receivers are combined to cancel common errors to achieve highly precise relative measurements. However, for an arbitrarily large swarm of N satellites, the number of measurements that are required for dGNSS grows as N^2. This easily becomes computationally infeasible for real-time applications on CubeSats. Thus, a different approach must be used to reduce the computational load which incurs especially during the measurement update of the EKF.

The new navigation strategy employed in DiGiTaL is to split the full orbit determination into two main modules, referred to as DiGiTaL's Orbit Determination (DOD) and Swarm Determination (DSD). For each user satellite, 1 to 2 partner satellites are chosen for DOD. GNSS measurements are shared between each of these satellites, and an EKF onboard the user utilizes dGNSS to estimate the states of all spacecraft within this subset. This estimate information is then shared with the rest of the swarm through the ISL and fused by DSD to create full swarm orbit knowledge onboard each spacecraft. The partnerships between the spacecraft in the swarm are directed, meaning that Satellite A being a partner of Satellite B does not mean that Satellite B is a partner of Satellite A. The resulting graph must also be connected to ensure that DSD has enough information to reconstruct the entire swarm state. These segments are discussed in detail in the following subsections. In this work, the topology of the network is set beforehand by design. To determine the satellite partnerships for DOD, the potential accuracy of the relative state estimate between each pair can be analyzed a-priori. This strictly depends on the number of single-difference carrier-phase measurements that can be formed, and therefore on the number of commonly visible GNSS satellites. Partnerships can then be decided by analyzing each attitude mode foreseen for the mission and by defining pairs that maximize the number of commonly visible satellites.

The high-level block diagram of the DiGiTaL software architecture is shown in Figure 4. The system receives GNSS data (timing information, raw measurements and ephemerides), attitude and maneuver information from the local GNSS receiver and the Attitude and Orbit Control System (AOCS), respectively. This information is processed in the DiGiTaL Data Interface (DDIF) block, which also receives the same information from the partner satellites (remote satellites in the same subset) via the ISL. This block checks that local and remote GNSS data form sets of synchronous valid measurements and passes this information to DOD. DDIF also receives the GNSS receiver's navigation solutions, which are used for quick initialization of the EKF. DOD provides the state and covariance of the local and partner spacecraft to DSD which also receives the subset estimates from all remote spacecraft through the ISL. In turn, DSD fuses all state and covariance estimates of the connected spacecraft to form a full swarm estimate. This output is passed to the DiGiTaL Orbit Prediction (DOP) block. Due to their computational complexity, DOD and DSD are executed at a slow rate of 0.033 Hz (30s sample time) which might be less than required by an onboard user. Therefore, DOP has the task to extrapolate the swarm state and covariance for provision to the user at a higher frequency of 1 Hz. Each block produces telemetry for downlink and receives telecommands to set operations parameters.
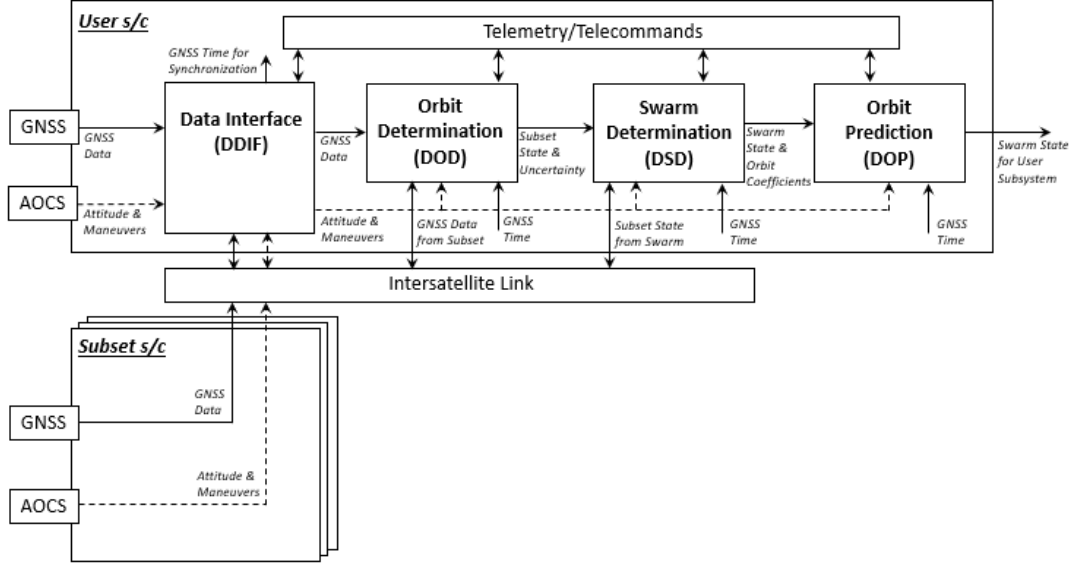
Figure 4: DiGiTaL **s**oftware architecture block diagram

Orbit Determination

To determine the spacecraft states within DOD, a multi-inertial EKF estimates the absolute states of each spacecraft within a given subset of the swarm. Each spacecraft of the subset broadcasts its local GNSS measurements and auxiliary data, and each user spacecraft forms combinations of the received datatypes to perform dGNSS. The native pseudorange and carrier-phase measurements produced by the receiver are modeled as

$$\rho_{pr}(t) = \|\mathbf{r}(t) - \mathbf{r}_{GNSS}(t - \tau)\| + c(\delta t - \delta t_{GNSS}) + I + \epsilon_{pr} \tag{1}$$
$$\rho_{cp}(t) = \lambda\Phi = \|\mathbf{r}(t) - \mathbf{r}_{GNSS}(t - \tau)\| + c(\delta t - \delta t_{GNSS}) - I + \lambda N + \epsilon_{cp}$$

In this formulation, $\mathbf{r}$ is the position vector of the user's antenna and $\mathbf{r}_{GNSS}$ is the position vector of the GNSS satellite's antenna (specifically the phase center of the antennae). The clock offset of both the receiver and the GNSS system are given by δt and δt_{GNSS}, respectively. This model includes the effects of signal time-of-flight, τ, ionospheric path delay, I, the carrier-phase integer ambiguities, N, multiplied by the wavelength of the incoming signal, λ, and the receiver-specific noise values, ϵ_{pr} and ϵ_{cp}. Receiver and channel dependent biases as well as phase wind-up on the carrier-phase have been neglected in Equation 1.

Two types of measurement combinations are used in the DiGiTaL framework. The first is an absolute measurement that is the arithmetic average of the raw pseudorange and carrier-phase measurements, which eliminates the ionospheric path delays. This is known as the Group and Phase Ionospheric Calibration (GRAPHIC) [30], and is given by

$$\rho_{gr}(t) = \frac{\rho_{pr}(t) + \rho_{cp}(t)}{2} = \|\mathbf{r}(t) - \mathbf{r}_{GNSS}(t - \tau)\| + c(\delta t - \delta t_{GNSS}) + \lambda\frac{N}{2} + \epsilon_{gr} \tag{2}$$

where $\epsilon_{gr} \approx \epsilon_{pr}/2$.

The second measurement type that DiGiTaL uses is the single-difference carrier-phase (SDCP) measurement, which provides a precise knowledge of the baseline between the receivers. SDCP is formed by differencing two synchronous carrier-phase measurements to the same GNSS satellite produced by two partner satellites in the subset. This measurement type eliminates common errors such as broadcast ephemeris errors, GNSS clock offset, and ionospheric path delays when considering small separations. The SDCP is modeled by

$$\rho_{sdcp}^{uw}(t) = \rho_{cp}^{u}(t) - \rho_{cp}^{w}(t) = \|\mathbf{r}(t) - \mathbf{r}_{GNSS}(t - \tau)\|^{uw} + c\delta t^{uw} + \lambda N^{uw} + \epsilon_{sdcp} \tag{3}$$

where u and w represent two different receivers, and $(\cdot)^{uw} = (\cdot)^{u} - (\cdot)^{w}$. In the case of uncorrelated carrier-phase measurements $\epsilon_{sdcp} \approx \sqrt{2}\epsilon_{cp}$, thus the common error cancellation comes at a cost of higher measurement noise.

Each DOD instance on the user satellite processes GRAPHIC measurements of itself and its partner satellites, as well as SDCP measurements between each pair of satellites in the subset. Measurements from each GNSS constellation and frequency are processed identically. The resulting measurement vector for a subset of three satellites is given by

$$\mathbf{z} = [\boldsymbol{\rho}_{gr}^{u} \quad \boldsymbol{\rho}_{gr}^{v} \quad \boldsymbol{\rho}_{gr}^{w} \quad \boldsymbol{\rho}_{sdcp}^{uv} \quad \boldsymbol{\rho}_{sdcp}^{uw} \quad \boldsymbol{\rho}_{sdcp}^{vw}]^{T} \tag{4}$$

which consists of a set of GRAPHIC measurements for satellites u, v, and w, and a set of SDCP measurements between each pair. While the inclusion of the partner satellites' GRAPHIC measurements in addition to the SDCP provides redundancy, it was found that this combination provides better navigational performance than including only the user's GRAPHIC measurements. In addition to the inertial position and velocity of each spacecraft, the estimation state of the filter must also include the carrier-phase bias of each tracked signal, and the clock offset of each receiver. Since DiGiTaL uses signals from multiple GNSS constellations that are not time synchronized, a receiver clock offset for each constellation must be considered. This gives a full state vector as

$$\mathbf{x} = [\mathbf{r}^{u} \quad \mathbf{v}^{u} \quad \mathbf{a}_{emp}^{u} \quad \mathbf{c\delta t}^{u} \quad \mathbf{N}^{u} \quad \mathbf{r}^{v} \quad \mathbf{v}^{v} \quad \mathbf{a}_{emp}^{v} \quad \mathbf{c\delta t}^{v} \quad \mathbf{N}^{v} \quad \mathbf{r}^{w} \quad \mathbf{v}^{w} \quad \mathbf{a}_{emp}^{w} \quad \mathbf{c\delta t}^{w} \quad \mathbf{N}^{w}]^{T} \tag{5}$$

where $\mathbf{r}$ and $\mathbf{v}$ are the position and velocity of each spacecraft center of mass in the Earth-Centered Inertial (ECI) frame and $\mathbf{a}_{emp}$ is the empirical acceleration vector aligned in the radial R, along-track T, and cross-track N directions. The clock offset and carrier-phase bias vectors are given by $\mathbf{c\delta t}$ and $\mathbf{N}$, respectively.

The filter estimates the carrier-phase biases as float values for initialization. Float estimation allows for relative positioning knowledge at about 10 cm as shown in the PRISMA mission [13]. Once the filter has reached steady state, IAR is activated to fix the real-valued biases to integer values. This allows for exploitation of the low noise on the carrier-phase measurements to achieve (sub-)centimeter-level relative positioning knowledge. IAR occurs after the measurement update has been completed and tries to fix the ambiguities prior to the next time update. DiGiTaL uses the Modified Least-Squares Ambiguity Decorrelation (mLAMBDA) method [31], which takes as inputs a vector of double-differenced carrier-phase (DDCP) ambiguities and their corresponding covariance and outputs the integer-fixed vector of those same ambiguities. DDCP measurements are formed by differencing SDCP measurements taken from different GNSS satellites, given as

$$\rho_{ddcp}^{uw}(t) = \rho_{kl}^{uw}(t) = \rho_{k}^{uw}(t) - \rho_{l}^{uw}(t) = \|\mathbf{r}(t) - \mathbf{r}_{GNSS}(t-\tau)\|_{kl}^{uw} + \lambda N_{kl}^{uw} + \epsilon_{ddcp} \tag{6}$$

where the subscripts k and l denote different GNSS satellites and $(\cdot)_{kl}^{uw} = (\cdot)_{k}^{uw} - (\cdot)_{l}^{uw}$. Figure 5 provides a diagram of the IAR process used in DiGiTaL, where ambiguities marked with a tilde are float values, and those without are integer-fixed.
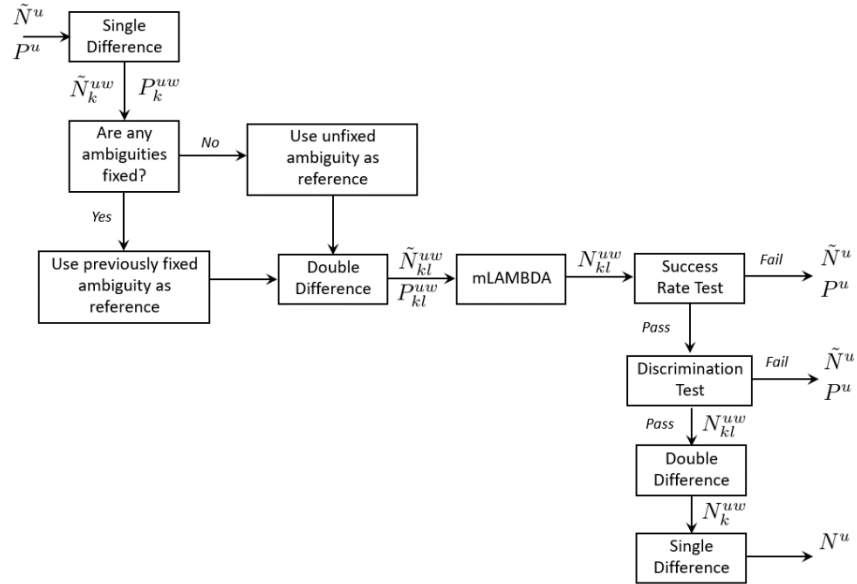

Figure 5: Flow-chart describing the Integer Ambiguity Resolution process for DiGiTaL between satellites $\boldsymbol{u}$ and $\boldsymbol{w}$

The undifferenced float ambiguities $\widetilde{N}^u$ in the state vector are used to form single-difference float ambiguities $\widetilde{N}_k^{uw}$ by differencing ambiguities from the same GNSS satellite on two receivers. The same linear transformation is applied to the associated covariance matrix P to form its single-difference equivalent. Double-difference ambiguities $\widetilde{N}_{kl}^{uw}$ are formed by differencing $\widetilde{N}_{SD}$, with one $\widetilde{N}_k^{uw}$ chosen as a reference for each difference to be made against. This reference is chosen from the ambiguities that have already been fixed to remove further uncertainty. If no ambiguity has been fixed yet, the $\widetilde{N}_k^{uw}$ with the highest elevation is chosen as a reference. The mLAMBDA method takes the $\widetilde{N}_{kl}^{uw}$, decorrelates them from one another as much as possible, and performs a search to find appropriate integer vectors. Once the integer vector is found, a series of checks are applied to ensure that it is valid. The first test provides a lower-bound to the success rate, and if this value is above a threshold, then the test is passed [32]. This lower bound is given by

$$Prob > \prod_{i=1}^n \left(1 - e^{\frac{-1}{2}\left(\frac{1}{2\sigma_{i|I}}\right)^2} \right)^{\frac{1}{2}} \tag{7}$$

where n is the number of ambiguities being fixed, $\sigma_{i|I}$ is the uncertainty on ambiguity i conditioned on all previous fixed ambiguities $I = 1, \ldots, i-1$. For DiGiTaL, if this probability is above 0.99, the test is considered passed. The second test is known as the Discrimination Test and compares the likelihood of the output solution with the second-best solution that the mLAMBDA method found [33]. This likelihood is given as

$$R = \left(\widetilde{N}_{kl}^{uw} - N_{kl}^{uw} \right)^T (P_{kl}^{uw})^{-1} \left(\widetilde{N}_{kl}^{uw} - N_{kl}^{uw} \right) \tag{8}$$

which is evaluated for both the best solution R_B and the second best R_S. The test is passed if

$$\frac{R_S}{R_B} > k \tag{9}$$

where k is a positive scalar set to 3 in DiGiTaL. Upon successful testing through Equations 7-9, the ambiguities are considered fixed and thus treated deterministically. All corresponding entries in the covariance are set to zero to reflect this. This is held true until the GNSS satellite is no longer tracked, at which point that ambiguity is reinitialized. When a new satellite is tracked, a few filter iterations are waited until the bias estimate has come to reach steady state before fixing it. This has been found to decrease improper fixing compared with attempting to fix immediately.

Once the ambiguities are fixed, new measurement residuals are calculated, and a final check is performed, referred to as the Residual Check. If any of the SDCP residuals are greater than half of the wavelength of the signal, then it can be assumed that the corresponding ambiguities on that measurement were improperly fixed. This is because at steady-state, the SDCP residuals should be on the order of the noise of that measurement, which is ~1mm. One of the ambiguities can then be adjusted to reduce that residual to the expected range. It was found that this check prevented degradation of the filter in some cases.

The time update of the filter is performed by numerically integrating both the state and variational equations of motion in inertial space [6]. However, the computational load of this method restricts the fidelity of the propagation, and a reduced-dynamics model is used. This model can be specified by the user and tailored to the environment faced by the spacecraft. Nominally, the dynamics model includes the GGM01S gravity model, up to degree and order 20 [34]. To improve the propagation, the empirical accelerations estimate unmodeled dynamics such as solar radiation pressure and third-body effects, and they are included in the equations of motion. These state variables are modeled as first-order Gauss-Markov processes, with the variance given as

$$q_i = \sigma_i^2 \left(1 - e^{-\frac{2\Delta t}{\tau_i}} \right) \tag{10}$$

which is added to the filter as process noise. In this model, σ is the standard deviation of that component of the empirical acceleration, Δt is the time step of the filter, and τ is the auto-correlation time constant. The carrier-phase biases are treated as constants during the time update, and the receiver clock offsets are modeled as random-walk processes, with the variance modeled as

$$q_i = \frac{\sigma_i^2 \Delta t}{\tau_i} \tag{11}$$

Swarm Determination

The goal of DSD is to provide relative orbit knowledge of all connected spacecraft relative to the user satellite. To this end, DSD fuses the orbit estimates provided by all DOD instances across the swarm. To reduce the amount of data sent through the ISL, DOD forms relative states (position and velocity) between the partner satellites prior to broadcasting as

$$\Delta \mathbf{x}_{BA} = \mathbf{x}_B - \mathbf{x}_A \qquad (12)$$
$$\Delta \mathbf{P}_{BA} = \mathbf{P}_A + \mathbf{P}_B - \mathbf{P}_{AB} - \mathbf{P}_{BA}$$

where subscripts A and B denote different satellites of the subset at hand, and AB represents the cross-correlation terms of the covariance. Sending the relative state and covariance defined by Equation 12 reduces the number of parameters to be sent from 156 for a subset of 2 satellites (12 element state with a 12x12 covariance) to 44 (6 element state with a 6x6 covariance). DSD receives this data from all subsets and fuses it to produce full swarm relative orbit knowledge. This is done using two approaches that can be selected via telecommand. The first method uses plain vector algebra across the connected graph to solve for the states of all swarming spacecraft. An illustrative example is shown in Figure 6 for a swarm of four spacecraft split in subsets of two units each.
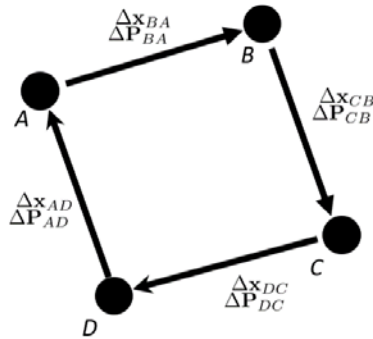
User Spacecraft	Partner Spacecraft	DOD Output by User
A	B	$\Delta \mathbf{x}_{BA}, \Delta \mathbf{P}_{BA}$
B	C	$\Delta \mathbf{x}_{CB}, \Delta \mathbf{P}_{CB}$
C	D	$\Delta \mathbf{x}_{DC}, \Delta \mathbf{P}_{DC}$
D	A	$\Delta \mathbf{x}_{AD}, \Delta \mathbf{P}_{AD}$

Figure 6: Swarm example with tabulated graph information. Arrows indicate partnership (i.e., B is a partner of A).

In this example, DSD is receiving the DOD output listed in Figure 6 (column 3) which is based on dGNSS processing between the satellites in subscript. Although the relative states between directly connected spacecraft are readily available and can be passed through without loss of accuracy, DSD needs to compute the missing relative states without profiting from explicit error cancellation through differential carrier-phase measurements. This is simply done by adding the available relative states (from A to B and B to C) as

$$\Delta \mathbf{x}_{CA} = \Delta \mathbf{x}_{BA} + \Delta \mathbf{x}_{CB} \qquad (13)$$

The estimated covariance of this estimate is given by

$$\Delta \mathbf{P}_{CA} = \Delta \mathbf{P}_{BA} + \Delta \mathbf{P}_{CB} \qquad (14)$$

There is no known information about the cross-correlation between these added states, and therefore Equation 14 does not take this into account. However, an alternative path to evaluate Equations 13-14 is given by

$$\Delta \mathbf{x}_{CA} = -\Delta \mathbf{x}_{AD} - \Delta \mathbf{x}_{DC} \qquad (15)$$
$$\Delta \mathbf{P}_{CA} = \Delta \mathbf{P}_{AD} + \Delta \mathbf{P}_{DC}$$

which can be merged with Equations 13-14 through arithmetic averaging or covariance intersection to improve the cancellation of common error modes.

To improve accuracy, a second approach is used by DiGiTaL which is based on a Kinematic Kalman Filter (KKF) [35]. The state includes the position, velocity, and acceleration of all swarming spacecraft relative to the user, while the DOD outputs (see Figure 6, column 3) are treated as pseudo-measurements with associated noise covariance given by the DOD delivered state covariance information. The choice of a kinematic filter virtually de-correlates the otherwise highly auto-correlated pseudo-measurements which are produced by a reduced-dynamics orbit determination (DOD's EKF) themselves. A

basic implementation of the KKF is provided in the following for a pair of satellites along axis i with $\boldsymbol{x} = (\Delta r_i, \Delta v_i, \Delta a_i)$. The state update equation is given by

$$x(k+1) = \boldsymbol{F}x(k) + \boldsymbol{v}(k) \tag{16}$$

where

$$\boldsymbol{F} = \begin{bmatrix} 1 & \Delta t & \frac{1}{2}\Delta t^2 \\ 0 & 1 & \Delta t \\ 0 & 0 & 1 \end{bmatrix} \tag{17}$$

with Δt equal to the filter time step (30s). The process noise added to the filter is given by

$$\boldsymbol{Q} = \begin{bmatrix} \frac{1}{20}\Delta t^5 & \frac{1}{8}\Delta t^4 & \frac{1}{6}\Delta t^3 \\ \frac{1}{8}\Delta t^4 & \frac{1}{3}\Delta t^3 & \frac{1}{2}\Delta t^2 \\ \frac{1}{6}\Delta t^3 & \frac{1}{2}\Delta t^2 & \Delta t \end{bmatrix} \tag{18}$$

This approach is more computationally expensive than the deterministic vector algebra mode. However, it has the potential to optimally blend all available information provided by DOD.

VERIFICATION AND EVALUATION

The functionality and performance of DiGiTaL is evaluated at the Stanford GNSS and Radiofrequency Autonomous Navigation Testbed for DSS (GRAND) [25]. This testbed was designed to evaluate each aspect of small-satellite GNSS navigation systems in a hardware-in-the-loop environment, including the receiver, intersatellite radios, and flight software. A high-fidelity orbit and attitude propagator simulates the dynamic space environment, and the resulting translational and rotational trajectories are used in an IFEN GNSS signal simulator to realistically mimic the radiofrequency signals that a receiver would track in flight. A receiver that is stimulated by these signals can be characterized through comparison with the adopted reference truth, while the measurements generated by the receiver can be used in a navigation filter such as the one described in the previous section.

This paper documents a representative test of DiGiTaL accuracy. A four-satellite swarm was simulated in the high-fidelity propagator under a full-force model. Table 5 lists the key simulation parameters, including force models and spacecraft ballistic coefficients. The swarm was chosen to represent an advanced synthetic aperture radar interferometry mission including one large satellite transmitter (Sat 1), and three smaller, identical satellite receivers (Sats 2, 3 and 4).

Table 5: Simulation parameters. Sat 1's parameters are in the fourth column, first entry. Sats 2, 3 and 4's parameters are in the fourth column, second entry.

Force	Model	Spacecraft Parameter	Value
Gravity Field	GGM01S (120x120) [34]	Mass	10.775
Atmospheric Drag	Harris-Priester [36]		4.975
	Cannonball spacecraft model [36]	Effective Drag Area	0.06
Solar Radiation Pressure	Flat plat model [36]		0.01
	Conical Earth Shadow model [36]	Coefficient of Drag	2.3
Geomagnetic & Solar Flux Data	NOA Daily KP AP Indices		2.3
Third-Body Perturbations	Analytical Sun & Moon [36]	Effective SRP Area	0.06
	DE430 (All planets) [37]		0.06
Relativistic Corrections	First-order corrections for special	Coefficient of	1.8
	and general relativistic effects [36]	Reflectivity	1.8

The orbital elements of each spacecraft are listed in Table 6. These are LEO orbits and the relative motion is illustrated in Figure 7 in the RTN-frame centered at Sat 1. The simulation lasts 6 hours and includes GNSS signals from GPS L1, Galileo E1, and BeiDou B1. The GNSS signal simulation includes the effects of ionospheric path delay and broadcast ephemeris errors with respect to IGS precise products as from archived IGS data (meter level) [37].

Table 6: Absolute orbital elements of Sat 1, with the relative orbital elements of Sats 2, 3, and 4

| Absolute Orbital Elements	Satellite 1	Relative Orbital Elements	Satellite 2	Satellite 3	Satellite 4
Semi-Major Axis (a) [km]	7078.136	Relative Semi-Major Axis ($a\delta a$) [m]	0.00	0.00	0.00
Eccentricity (e) [-]	5×10^{-4}	Relative Mean Longitude ($a\delta\lambda$) [m]	0.00	-750.00	-1500.00
Inclination (i) [°]	98.188	Relative Eccentricity ($a\delta e_x$) [m]	0.00	-259.81	-259.81
Longitude of Ascending Node (Ω) [°]	0.552	Relative Eccentricity ($a\delta e_y$) [m]	300.00	-150.00	-150.00
Argument of Perigee (ω) [°]	0.01	Relative Inclination ($a\delta i_x$) [m]	0.00	-519.62	519.62
Mean Anomaly (M) [°]	0.02	Relative Inclination ($a\delta i_y$) [m]	600.00	-300.00	-300.00
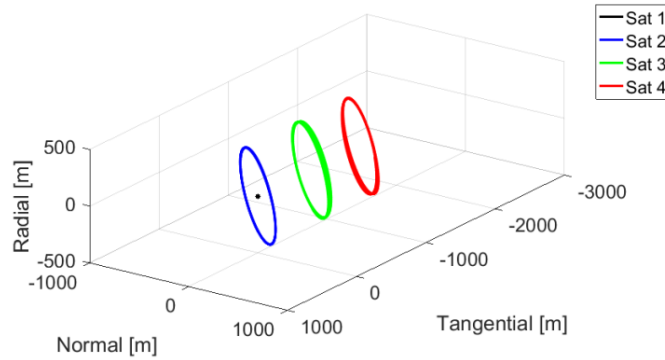
Figure 7: Relative orbits of each satellite in the RTN-frame of Sat 1

DiGiTaL is embedded in the Tyvak flatsats and its performance is evaluated by comparing the output of the DOD and DSD software modules with the reference truth from GRAND. Results are shown in Tables 8-10 and Figures 8-11. The connectivity of the swarm's graph is set through 4 subsets of two satellites each. Thus, each DOD filter instance estimates the state of the local satellite plus that of the other satellite in the subset (i.e., Sat 1 estimates Sat 1 and Sat 2). The reduced-dynamics model used in DOD includes the GGM01S gravity model up to 20 order and degree and empirical accelerations. The a-priori settings of DOD's EKF are listed in Table 7.

Table 7: A-priori settings of DOD's Extended Kalman Filter

Parameter	Value	Parameter	Value
A-priori standard deviation		*Process noise*	
σ_r [m]	1000	σ_{a_R} [nm/s^2]	7500
σ_v [m/s]	1	σ_{a_T} [nm/s^2]	1000
σ_{a_R} [nm/s^2]	1000	σ_{a_N} [nm/s^2]	500
σ_{a_T} [nm/s^2]	2000	$\sigma_{c\delta t}$ [m]	5
σ_{a_N} [nm/s^2]	750	σ_N [cycles]	0.1
$\sigma_{c\delta t}$ [m]	1000		
σ_N [cycles]	1	*Measurement standard deviation*	
		σ_{pr} [m]	0.250
Auto-correlation time scale		σ_{cp} [m]	0.005
τ_a [s]	900		
$\tau_{c\delta t}$ [s]	60		

Figure 8 shows the absolute positioning error of Sat 1, and the relative positioning error of Sat 2 with respect to Sat 1 expressed in the RTN frame of Sat 1. The associated statistics are given in Table 8. The statistics are calculated on the difference

between estimated and true state (thus reflecting actual performance), while the light error bounds shown in the filter plots represent the estimated covariance (1σ). The absolute positioning achieves errors of about 1 m (1D, rms), which is consistent with the broadcast ephemeris errors. The red vertical line indicates the initialization of IAR, at which point the relative positioning errors reduce from decimeter-level to about 1 cm (1D, rms). The associated formal covariance follows closely the actual error trend. During this period, it was found that 88% of ambiguities were fixed, with 1.4% being manually adjusted by the Residual Check.
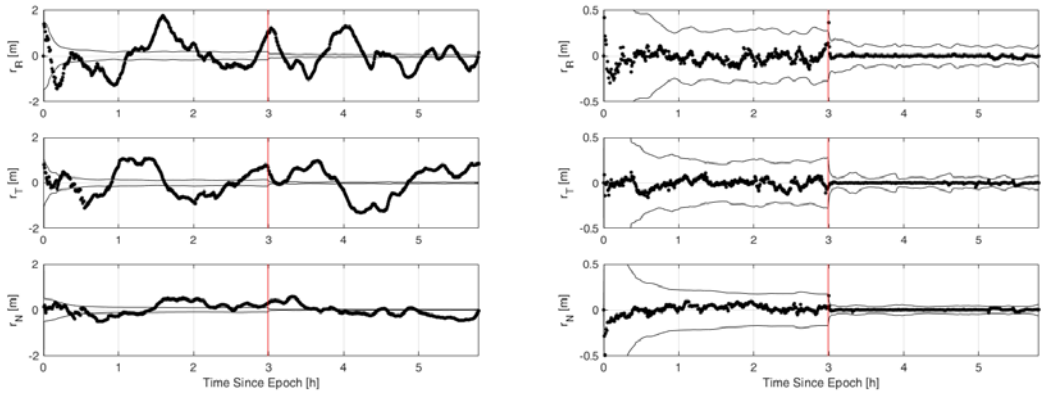

Figure 8: Absolute position error of Sat 1 (left) and relative position error of Sat 2 with respect to Sat 1 (right). Activation of IAR is shown by the red line.

The velocity estimate errors by DOD are plotted in Figure 9. These results show the same trends as the position, with absolute and relative velocity errors of 1 mm/s and 0.1 mm/s (1D, rms), respectively.
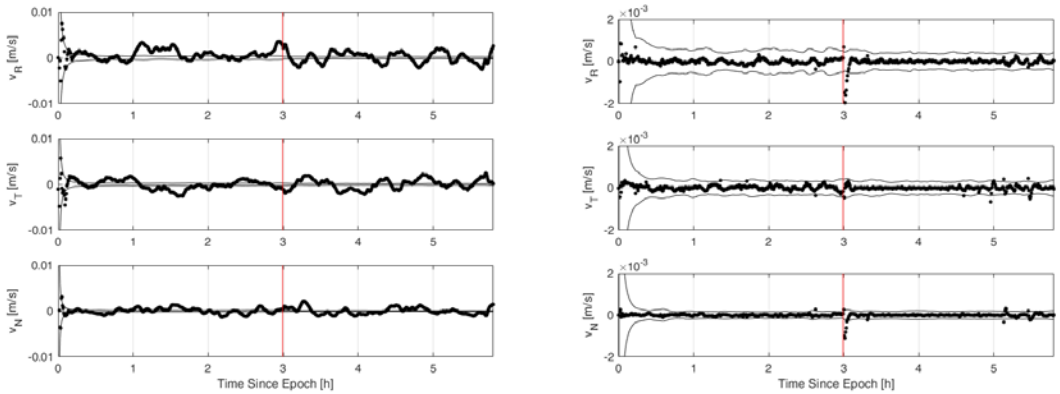

Figure 9: Absolute velocity error of Sat 1 (left) and relative velocity error of Sat 2 with respect to Sat 1 (right). Activation of IAR is shown by the red line.

Table 8: State estimate statistics for DOD. Absolute errors are listed in the left three columns. Relative errors are listed on the right three columns.

Absolute State	Without IAR	With IAR	Relative State	Without IAR	With IAR
r_R	-0.053 ± 0.693 m	0.029 ± 0.579 m	r_R	-0.025 ± 0.065 m	-0.001 ± 0.023 m
r_T	0.032± 0.611 m	0.054 ± 0.693 m	r_T	-0.008 ± 0.050 m	-0.002 ± 0.008 m
r_N	0.083 ± 0.269 m	-0.054 ± 0.254 m	r_N	0.012 ± 0.044 m	0.001 ± 0.011 m
v_R	0.738 ± 1.123 mm/s	0.108 ± 1.263 mm/s	v_R	-0.000 ± 0.109 mm/s	-0.021 ± 0.205 mm/s
v_T	-0.101 ± 1.051 mm/s	0.079 ± 1.121 mm/s	v_T	0.025 ± 0.107 mm/s	-0.001 ± 0.105 mm/s
v_N	0.009 ± 0.568 mm/s	0.027 ± 0.734 mm/s	v_N	0.000 ± 0.042 mm/s	-0.011± 0.116 mm/s

The post-fit residuals for each measurement type are plotted in Figure 10 to show the overall capability of the filter to fit the observations through the reduced-order dynamics model. Table 9 demonstrates how the standard deviation of each

measurement type is consistent with previous results from the zero-baseline tests of Figure 2. It is interesting to note the marked increase of noise of the SDCP residuals after activation of IAR. Indeed, DOD no longer has a free parameter to adjust on each measurement (float bias) to drive the residual to zero. However, the statistical properties are de-facto not affected due to the reduction of outliers after IAR.
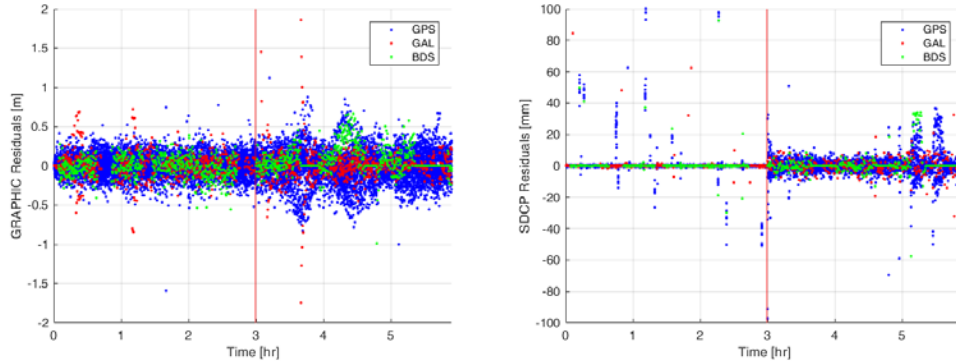

Figure 10: GRAPHIC (left) and SDCP (right) measurement residuals, with colors denoting GNSS constellations

Table 9: Measurement residual statistics for each measurement type and GNSS constellation

Measurement	Constellation	Without IAR	With IAR
GRAPHIC	GPS	0.0000 ± 0.1375 m	0.0000 ± 0.1804 m
	Galileo	0.0019 ± 0.1925 m	0.0027 ± 0.2112 m
	BeiDou	-0.0213 ± 0.1350 m	0.0750 ± 0.1659 m
SDCP	GPS	0.1900 ± 25.4089 mm	-0.2926 ± 21.5984 mm
	Galileo	0.4251 ± 5.7324 mm	-1.2906 ± 25.8497 mm
	BeiDou	1.0583 ± 9.9116 mm	0.5126 ± 13.3211 mm

DSD receives state estimates from all DOD instances of the swarm every 30s. From this received data, a full swarm state can be determined by using the vector algebra approach described in the previous section. A relative state to Sat 3 is calculated by adding the relative state of 3 with respect to 2 received from DOD on 2 ($\Delta\mathbf{x}_{32}$) to the output from DOD on 1 ($\Delta\mathbf{x}_{21}$). A relative estimate of Sat 4 is formed using the relative state of 1 with respect to 4 from DOD on 4 ($\Delta\mathbf{x}_{14}$). Figure 11 shows the full swarm state as estimated by Sat 1, and the statistics can be found in Table 10. When using vector algebra to calculate the relative state of Sat 3, there is an expected increase in the uncertainty, as seen by the covariance bounds. This becomes apparent when comparing it to the relative state of Sat 4, where no vector addition is performed ($\Delta\mathbf{x}_{41} = -\Delta\mathbf{x}_{14}$). However, this increase is not necessarily the case for the true error. As seen in Table 10, the estimate of $\Delta\mathbf{x}_{31}$ is more accurate than the estimate of $\Delta\mathbf{x}_{41}$ in some directions (i.e., r_R, r_N, and v_T before IAR). The increase of uncertainty is due to the unknown cross-correlations between the added states, which motivates the use of a KKF which will be documented in upcoming publications. However, this method is computationally very efficient, and is effective for real-time applications.
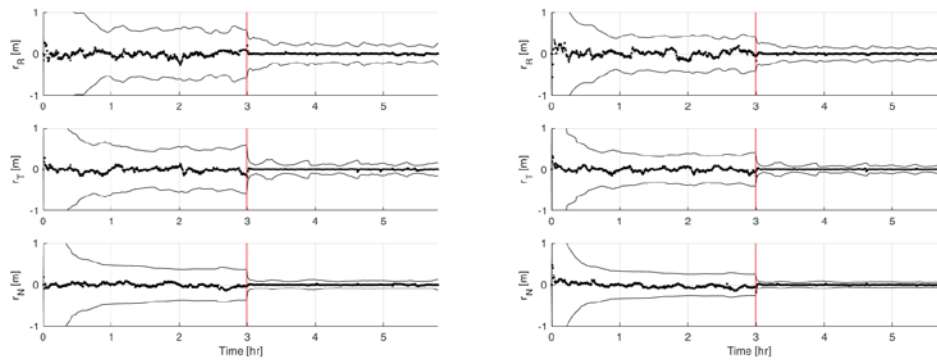

Figure 11: Relative position error of Sat 3 (left) and Sat 4 (right) with respect to Sat 1 through DSD

Table 10: Relative state estimate statistics from DSD

3-1	Without IAR	With IAR	4-1	Without IAR	With IAR
r_R	-0.009 ± 0.066 m	0.001 ± 0.015 m	r_R	0.016 ± 0.078 m	0.002 ± 0.012 m
r_T	-0.016 ± 0.056 m	-0.001 ± 0.014 m	r_T	-0.008 ± 0.051 m	0.001 ± 0.010 m
r_N	-0.005 ± 0.044 m	0.000 ± 0.007 m	r_N	0.019 ± 0.052 m	-0.000 ± 0.011 m
v_R	0.017 ± 0.149 mm/s	-0.011 ± 0.147 mm/s	v_R	-0.001 ± 0.160 mm/s	0.007 ± 0.104 mm/s
v_T	-0.009 ± 0.074 mm/s	0.013 ± 0.163 mm/s	v_T	0.020 ± 0.084 mm/s	0.015 ± 0.135 mm/s
v_N	0.002 ± 0.049 mm/s	0.001 ± 0.066 mm/s	v_N	0.001 ± 0.052 mm/s	0.012± 0.123 mm/s

CONCLUSIONS AND FUTURE WORK

This work presents the design of the Distributed Multi-GNSS Timing and Localization system for nanosatellite swarm navigation. DiGiTaL uses Commercial-off-the-Shelf hardware components to provide arbitrarily large spacecraft formations with centimeter-level relative positioning accuracy through differential GNSS techniques. The system includes two Tallysman GNSS antennas and a NovAtel GNSS receiver, each selected to minimize mass and power while being compatible with the full range of GNSS signals available. The receiver is conditioned using a Chip-Scale Atomic Clock that provides a 10MHz reference signal, providing higher levels of synchronization throughout the swarm and reducing clock-drift in GNSS-impaired scenarios. The DiGiTaL flight software is embedded on an 800MHz Endeavour microprocessor, which is packaged as part of a Tyvak flatsat prototype. The flatsat also includes the NovAtel receiver and UHF radio, allowing multiple units to exchange measurements and state information in a hardware-in-the-loop testing environment.

The navigation software exploits the low-noise carrier-phase measurements to perform differential GNSS between multiple satellites. However, this method becomes a computational burden as the swarm grows. Therefore, DiGiTaL divides the swarm into subsets of two to three satellites where dGNSS is used for orbit determination. Synchronous GNSS measurements are sent within each subset, and an Extended Kalman Filter estimates the inertial states of each spacecraft. The mLAMBDA method fixes the integer ambiguities of each measurement, resulting in state estimates with relative-positioning accuracies on the centimeter-level. These subset estimates are shared with the rest of the swarm, and a full-swarm state can be constructed through a deterministic or kinematic filtering method. Each spacecraft is performing identical calculations, creating a decentralized network that resolve to the same relative swarm state.

The DiGiTaL prototype was evaluated in Stanford's GRAND hardware-in-the-loop testbed. A high-fidelity orbit propagator simulated a four-spacecraft swarm, and an IFEN GNSS signal simulator generated realistic measurements. Orbit determination results demonstrated navigation accuracies of <1 m and <1 cm for absolute and relative position, respectively, and swarm determination showed relative position accuracies with similar accuracy, as well as an increase in uncertainty when adding relative states through vector algebra due to unknown cross-correlation.

DiGiTaL is undergoing extensive testing, both at Stanford as well as in Goddard Spaceflight Center's Formation Flying Testbed. This testing campaign provides more opportunities to test multiple aspects of DiGiTaL, including studies of the antenna system to characterize gain patterns. Further algorithmic development includes investigations into different swarm determination methods, such as covariance intersection to fuse the incoming orbit determination estimates. More advanced Integer Ambiguity Resolution techniques will also be considered, such as constraining the search process through injection of the estimated baseline. These improvements to the DiGiTaL system will aid in robustness and achievable accuracy, with the goal of providing nanosatellite swarms with the utmost confidence in the provided navigation solutions.

ACKNOWLEDGMENTS

REFERENCES
[1] B. Sullivan, D. Barnhart, L. Hill, P. Oppenheimer, B. L. Benedict, G. Van Ommering, L. Chappell, J. Ratti, and P. Will, "DARPA phoenix payload orbital delivery system (PODs): FedEx to GEO" *AIAA SPACE 2013 Conference and Exposition*, San Diego, California, 2013, p. 5484.
[2] J. Kolmas, P. Banazadeh, A. W. Koenig, B. Macintosh, and S. D'Amico, "System design of a miniaturized distributed occulter/telescope for direct imaging of star vicinity," *2016 IEEE Aerospace Conference*, Big Sky, Montana, 2016, pp. 1-11.

[3] O. Montenbruck, G. Allende-Alba, J. Rosello, M. Tossaint, and F. Zangerl, "Precise Orbit and Baseline Determination for the SAOCOM-CS Bistatic Radar Mission," *Proceedings of the 2017 International Technical Meeting of The Institute of Navigation*, Monterey, California, January 30 – February 2, 2017. pp. 123-131.

[4] S. D'Amico, J.S. Ardaens, S. De Florio, O. Montenbruck, S. Persson, and R. Noteborn. "GPS-based spaceborne autonomous formation flying experiment (SAFE) on PRISMA: initial commissioning." *AIAA/AAS Astrodynamics Specialist Conference.* Toronto, Canada, August 2-5, 2010.

[5] R. Kroes, *Precise relative positioning of formation flying spacecraft using GPS*. PhD thesis, TU Delft, Delft University of Technology, 2006.

[6] S. D'Amico, *Autonomous Formation Flying in Low Earth Orbit*. PhD thesis, TU Delft, Delft University of Technology, 2010.

[7] B. Tapley, S. Bettadpur, M. Watkins, and C. Reigber. "The Gravity Recovery and Climate Experiment: Mission Overview and Early Results". *Geophysical Research Letters*, Vol. 31 No. 9, L09 607. May 2004.

[8] W. Bertiger, Y. Bar-Sever, S. Desai, C. Dunn, B. Haines, G. Kruizinga, D. Kuang, S. Nandi, L. Romans, M. Watkins, S. Wu, and S. Bettadpur. "Grace: Millimeters and Microns in Orbit", *Proceedings of ION GPS 2002*, Portland, Oregon, September 24-27, 2002. pp .2022–2029.

[9] G. Krieger, A. Moreira, H. Fiedler, I. Hajnsek, M. Werner, M. Younis, M. and Zink. "TanDEM-X: A Satellite Formation for High Resolution SAR Interferometry". *IEEE Transactions Geoscience and Remote Sensing*, Vol. 45, No. 11, pp. 3317–3341. November 2007.

[10] H. Fiedler, G. Krieger, M. Werner, K. Reiniger, E. Diedrich, M. Eineder, S. D'Amico, and S. Riegger "The TanDEM-X Mission Design and Data Acquisition Plan," *Proceedings of the 6th European Conference on Synthectic Aperture Radar*, Dresden, Germany, 2006.

[11] L. Winternitz, W. Bamford, S. Price, J. Carpenter, A. Long, and M. Farahmand. "Global Positioning System Navigation Above 76,000 km for NASA's Magnetospheric Multiscale Mission," *Navigation,* Vol. 64, No. 2, pp.289-300. June 2016.

[12] M. Farahmand, A. Long, and R. Carpenter. "Magnetospheric Multiscale Mission Navigation Performance Using the Goddard Enhanced Onboard Navigation System," *Proceedings of the 25th International Symposium on Space Flight Dynamics.* Munich, Germany, October 19-23, 2015.

[13] S. D'Amico, J.-S. Ardaens, and R. Larsson, "Spaceborne Autonomous Formation-Flying Experiment on the PRISMA Mission," *Journal of Guidance, Control, and Dynamics*, Vol. 35, No. 3, pp. 834-850, 2012.

[14] S. D'Amico, S. De Florio, J.S. Ardaens, T. Yamamoto. "Offline and hardware-in-the-loop validation of the GPS-based real-time navigation system for the PRISMA formation flying mission," *3rd International Symposium on Formation Flying, Missions and Technology*, Noordwijk, Netherlands. April 23, 2008. pp. 23-25.

[15] N. Roth, *Navigation and Control Design for the CanX-4/-5 Satellite Formation Flying Mission*, PhD thesis, University of Toronto, 2010.

[16] G. Bonin, N. Roth, S. Armitage, J. Newman, B. Risi, and R. Zee, "CanX-4 and CanX-5 Precision Formation Flight: Mission Accomplished!," *Proceedings of the 29th Annual AIAA/USU Conference on Small Satellites*, Logan, UT, 2015.

[17] J.-S. Ardaens, O. Montenbruck, and S. D'Amico, "Functional and performance validation of the PRISMA precise orbit determination facility," *ION International Technical Meeting*, San Diego, California, 2010, pp. 25-27.

[18] B. Ju, D. Gu, T. A. Herring, G. Allende-Alba, O. Montenbruck, and Z. Wang. "Precise orbit and baseline determination for maneuvering low earth orbiters." *GPS solutions* Vol. 21, No. 1, 2017, pp. 53-64.

[19] S. Bandyopadhyay, G. P. Subramanian, R. Foust, D. Morgan, S.-J. Chung, and F. Hadaegh, "A review of impending small satellite formation-flying missions," *53rd AIAA Aerospace Sciences Meeting*, Kissimmee, Florida, 2015, p. 1623.

[20] Roscoe, C., Westphal, J.J., and Bowen, J.A. "Overview and GNS Design of the CubeSat Proximity Operations Demonstration (CPOD) Mission", *9th International Workshop on Satellite Constellations and Formation Flying*, University of Colorado Boulder, CO, 2017.

[21] O. Montenbruck and R. Kroes, "In-Flight Performance Analysis of the CHAMP BlackJack GPS Receiver," *GPS Solutions*, Vol. 7, No. 2, 2003, pp. 74-86.

[22] O. Montenbruck, M. Garcia-Fernandez, and J. Williams, "Performance Comparison of Semicodeless GPS Receivers for LEO Satellites," *GPS Solutions*, Vol. 10, No. 4, 2006, pp. 249-261.

[23] N. Roth, B. Risi, C. Grant, and R. Zee, "Flight Results from The CanX-4 And CanX-5 Formation Flying Mission," *Proceedings of Small Satellites Systems and Services – The 4S Symposium*, Valletta, Malta, 2016.

[24] S. D'Amico, R. C. Hunter, and C. Baker, "Distributed Timing and Localization (DiGiTaL)," ARC-E-DAA-TN45564, 2017.

[25] Giralo V., D'Amico S.; *Development of the Stanford GNSS Navigation Testbed for Distributed Space Systems*; Institute of Navigation International Technical Meeting, Reston, Virginia, January 29- February 1, 2018.

[26] Tallysman, "A Tallysman *Acutenna* TW3972E High Gain Embedded Triple Band GNSS Antenna + L-band Correction Services," datasheet, 2016.

[27] NovAtel, "OEM 628 High Performance GNSS Receiver," D15588 datasheet, October 2016.

[28] P. Ward, *Satellite Signal Acquisition and Tracking, in Understanding GPS, Principle and Applications*. Kaplan, 2006.

[29] Jackson Labs, "Low Power Miniature RSR CSAC Time and Frequency Standard," 1005120 datasheet, July 2017.

[30] T. Yunck, *Coping with the Atmosphere and Ionosphere in Precise Satellite and Ground Positioning in: Environmental Effects on Spacecraft Trajectories and Positioning*. Washington, D.C., American Geophysical Union, 1993.

[31] X. W. Chang, X. Wang, and T. Zhou, "MLAMBDA: a modified LAMBDA method for integer least-squares estimation," *Journal of Geodesy*, Vol. 79, No. 9, 2005, pp. 552-565.

[32] S. Verhagen, *The GNSS Integer Ambiguities: Estimation and Validation*. PhD Thesis, TU Delft, Delft University of Technology, 2005.

[33] S. Verhagen, "Integer ambiguity validation: an open problem?", *GPS Solutions*, Vol. 8, No. 1, pp. 36–46, April 2004.

[34] B. D. Tapley, S. Bettadpur, M. Watkins, and C. Reigber, "The gravity recovery and climate experiment: Mission overview and early results," *Geophysical Research Letters*, Vol. 31, No. 9, 2004.

[35] Y. Bar-Shalom, X. R. Li, T. Kirubarajan. *Estimation with Applications to Tracking and Navigation: Theory Algorithms and Software.* Wiley and Sons, Inc. 2001, pp. 267 – 299.

[36] O. Montenbruck and E. Gill, *Satellite orbits*, Springer, Vol. 2, 2000, pp. 257-291.

[37] W. M. Folkner, J. G. Williams, D. H. Boggs, R. S. Park, and P. Kuchynka, "The planetary and lunar ephemerides DE430 and DE431," *Interplanet. Netw. Prog. Rep*, Vol. 196, 2014.

[38] J. M. Dow, R. E. Neilan, and C. Rizos, "The international GNSS service in a changing landscape of global navigation satellite systems," *Journal of Geodesy*, Vol. 83, No. 3, 2009, pp. 191-198.